Task 5A and 5B: Analytical model and Finite Element model to predict the test results

Evaluation of Glass Fiber Reinforced Polymer (GFRP) Spirals in Corrosion Resistant Concrete Piles

FDOT Contract Number: BDV30 977-27, FSU Project ID: 042924

Progress report date: 3/9/2023

Submitted to:

Florida Department of Transportation

Research Center

605 Suwannee Street

Tallahassee, Florida 32399-0450

Project Managers:

Christina Freeman	FDOT Structures Research Center
Ge Wan	FDOT Structures Design Office
Rodrigo Herrera	FDOT Structures Design Office

Prepared by:

Olayiwola Adegbulugbe	Graduate Research Assistant
Sungmoon Jung	Principal Investigator
Raphael Kampmann	Co-Principal Investigator

Department of Civil and Environmental Engineering

FAMU-FSU College of Engineering

2525 Pottsdamer St., Tallahassee, FL. 32310.

FAMU–FSU Engineering

TABLE OF CONTENTS

LIST OF FIGURES

LIST OF TABLES

Chapter 1.   Comparison of spiral design strength to test results

1.1 Introduction

The FDOT design for steel spirals in prestressed concrete piles are based on prescriptive methods. This design approach has proven to be adequate based on years of successful practice in which expected pile performance has been met. The main analytical model in this project used the force capacity by the FDOT design (that was proven to be adequate) combined with the force equilibrium. This model and experimental results will be discussed in Sections 1.2 and 1.3.

Additionally, the spiral force was predicted using the concrete core behavior. This approach led to excessive spiral force because it assumed complete failure/spalling of the outer concrete. However, since this model is commonly used it will also be discussed in Section 1.4.

1.2 GFRP Spiral design summary and prediction of spiral stress

Recall that details of the GFRP spiral design was discussed in Task 4B report, Section 3.2. Task 4B report also discussed the assumptions in the force equilibrium model used in the design:

- Quasi-static loading condition
- For the same axial loading, the steel spiral and the GFRP spiral experiences similar tensile force
- At the design requirement of 5 ksi concrete stress, the upper limit of the force was obtained by using the steel yield stress of 70 ksi. The corresponding spiral force was 2.38 kips.

A brief summary of the design approach given in Task 4B Section 3.2 is as follows. From the force equilibrium, the stress in the GFRP spiral will be:

$$\sigma = F_{spiral}/A_{CFRP} \qquad (1.1)$$

where A_{CFRP} is the cross-sectional area of the GFRP spiral and F_{spiral} is the tensile force in the spiral. By substituting the upper bound of the spiral force and the design requirement of 5 ksi concrete stress, i.e., 5×24^2 kips = 2880 kips axial force:

$$\sigma = \frac{2.38}{2880} F_{axial}/A_{CFRP} \qquad (1.2)$$

This equilibrium-based model can be used to predict the stress (and force) in the GFRP spiral.

1.3 Observed spiral force from impact tests vs predicted force and design tensile capacity

Recall, that PSG1 pile spiral was designed to match the tensile capacity of the PSS pile spiral. This capacity was calculated to be 2.38 kips. This design capacity was compared to the observed force in the spirals after impact force was applied to the pile from various drop heights. The force instead of the stress was used for an easier comparison between the steel and the GFRP spirals. The observed force was computed using the measured strain, elastic modulus, and cross-sectional area of the spiral. Table 1.1 and Table 1.2 summarize the axial force in the piles and the corresponding maximum spiral force in PSS and PSG1. In addition, a percentage of the spiral design capacity is also shown (with respect to the yield stress 70 ksi for PSS; strain limit of 0.006 for PSG1).

Table 1.1: Axial pile force and corresponding maximum spiral stress (PSS)

Drop heights (ft.)	Axial force (kips)	Observed max spiral force (kips)	Observed stress / yield stress (70 ksi) (%)
7	2124	0.17	7.1
15	3788	2.38	100

Table 1.2: Axial pile force and corresponding maximum spiral stress (PSG1)

Drop heights (ft.)	Axial force (kips)	Predicted max spiral force [Equation 1.2 × A] (kips)	Observed max spiral force (kips)	Observed strain / strain limit (0.006) (%)
4	976	0.81	0.70	16.3
7	1550	1.28	1.11	25.9
10	2468	2.04	1.77	41.3
15	2526	2.09	1.81	42.2
20	3272	2.70	2.34	54.5

Table 1.2 also has an additional column showing the predicted force using Equation 1.2. The prediction showed about 15% overestimation than the measured maximum force. The overestimation is expected because upper limit of the force (i.e., force corresponding to the yielded steel) was used in the design. However, the maximum observed force in the spiral almost reached the design capacity, so a decision was made for the next task (Task 6) to include a more conservative design as a possible alternative.

1.4 Prediction using the concrete core behavior

When a pile is subjected to an axial load, the concrete expands laterally due to the Poisson's effect. The lateral expansion of the concrete core is restrained by the spirals, which then causes a tensile stress on the spirals. The concrete core will be under triaxial compression due to the axial load and the restraint. Equations from this behavior is commonly used by researchers to relate the axial load and stresses in the concrete and the spiral, particularly to compute the maximum axial load.

However, the equations from the concrete core behavior will provide very large spiral force, because the approach assumes complete failure/spalling of the outer concrete while maintaining the load carrying capacity of the pile using the core of the concrete alone. Specifically, from Task 3 report (Section 1.2.1), the spiral area, concrete stress, and the spiral stress were related as:

$$A_{sh} = 0.3sh_c \left(\frac{A_g}{A_c} - 1\right)\frac{f_c'}{f_{yh}} \tag{1.3}$$

or,

$$A_{sh} = 0.09sh_c \frac{f_c'}{f_{yh}} \tag{1.4}$$

whichever is greater; where f_{yh} is the yield strength of spiral reinforcement, A_{sh} is the total cross-sectional area of transverse reinforcement in the direction considered, s is the spacing of tie sets in the longitudinal direction, and h_c is the width of the core in the direction considered. By using 5 ksi design requirement instead of f_c' and corresponding spiral stress σ instead of f_{yh}, the spiral stress and the force can be computed using Equations (1.3) and (1.4). The force in the spiral becomes about 6 kips, which is about 2.5 times greater than the approach explained in the previous section. The result is consistent with the earlier conclusion in the design stage (Task 4B report), i.e., spiral designed with this approach will be excessively large due to ignoring the outer concrete.

1.5 Limitations of the analytical model

The equilibrium-based model in section 1.2 was based on the design approach used in this project. The model overestimated the force in the spiral by about 15% compared to the experimental results. The model was simple and practical but lacked rigor in that it was based on empirical experience and prescribed design of the FDOT design guide.

The commonly used core behavior model fully explains the stress development in the axially loaded member, but it led to very large overestimation of the spiral force, because the approach assumed complete failure/spalling of the outer concrete. The approach will be useful at the ultimate loading condition but was not suitable for the purpose of this project.

The next section, finite element prediction, will fully account for all structural elements of the pile as well as dynamic loading effect.

Chapter 2.   Finite element model prediction

2.1 Background

Due to the highly complicated stress distribution during the pile impact, the analytical model alone would not be sufficient to predict the pile response. Although the analytical model was useful during the design stage, prediction of impact testing results will need to account for dynamic loading effect. This chapter will discuss the finite element model and its prediction of the testing results.

2.2 General model details

The impact loading of two prestressed concrete piles modeled using the finite element software ABAQUS are described and compared to the experimental impact loading results in this report. The prestressed concrete piles have a cross-section of 24 in. × 24 in. with a length of 28 ft. In addition to concrete, other materials modeled are steel strands, steel spirals and GFRP spirals. The properties and constitutive behavior these materials are in upcoming sections of this report. Dimensions and reinforcement details of the pile simulated under impact loading are shown in Figure 2.1 and Figure 2.2.
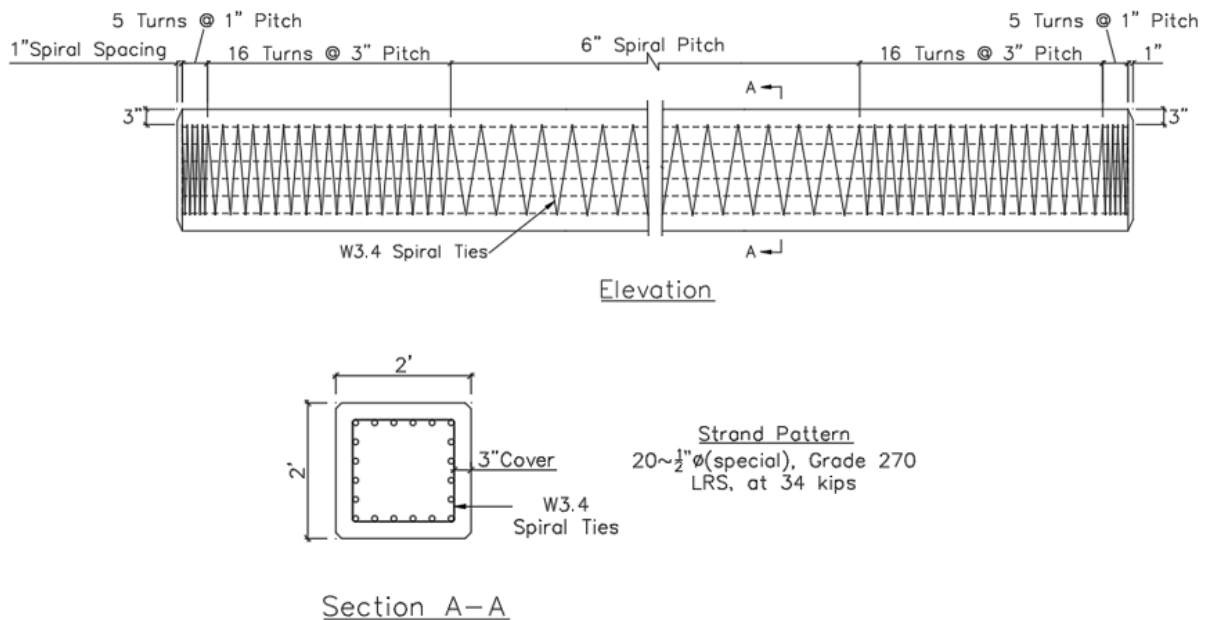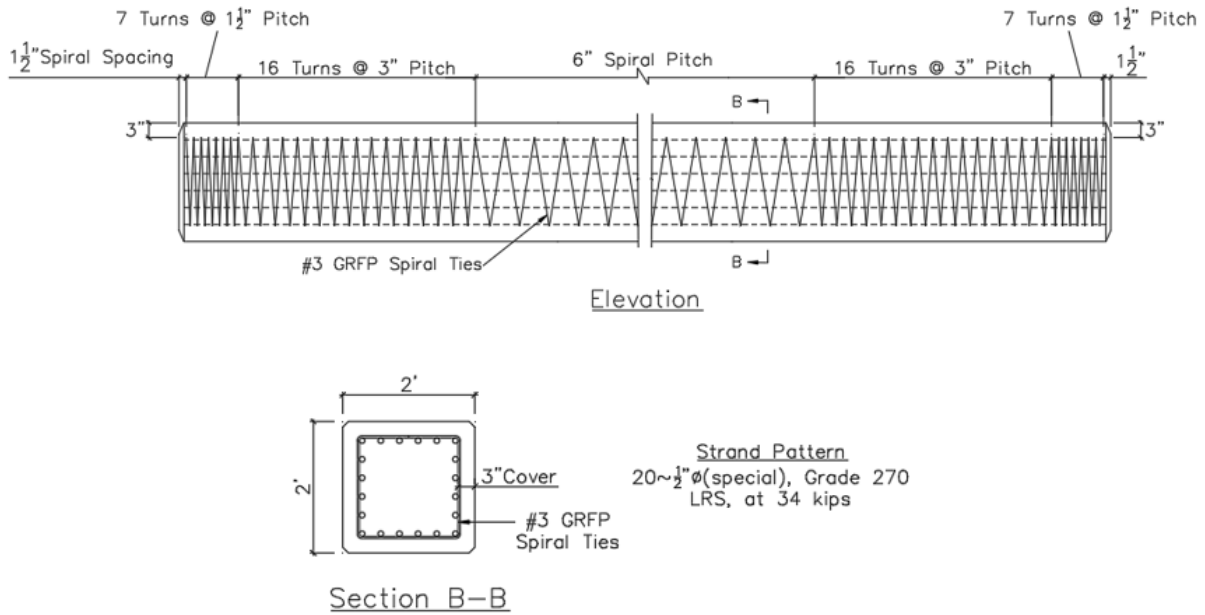

Figure 2.1: PSS details

Figure 2.2: PSG1 details

Test setup for the actual impact experiment has been well described in Task 4D report. In summary, the test setup consisted of an impactor attached to a pendulum mechanism, a pile placed longitudinally on steel supports overlayed with teflon. The teflon reduced friction between the pile and the supports which kept tested pile off the ground. In addition, plywood cushions were placed at the pile top and pile tip, and restraining blocks were placed at the tip of the piles to limit pile movement after impact.

In the finite element (FE) analyses, two modeling choices were made to run the dynamic analysis effectively. First, pile models were fixed at the tip as shown in Figure 2.3. This simplified model was utilized to limit the introduction of uncertainties resulting from the lack of actual measurement of the interaction between pile, support blocks, and soil. Second, the impact load was applied at the pile top directly rather than dropping it from a particular height via a pendulum mechanism. Both modeling choices would increase the impact energy on the pile, because of the lack of pile sliding and lack of the centripetal force action. Additional energy losses not included in the FE modeling include the tower vibration, cable vibration, closing of the gap between plywood cushions and the pile, and other miscellaneous energy loss such as heat, sound, etc.

Pile tip with
plywood cushion

Boundary
condition:
$U_X = U_Y = U_Z = 0$
$θ_X = θ_Y = θ_Z = 0$

(a)

Pile top with
plywood cushion

Impactor with
predefined velocity, V_{FE}

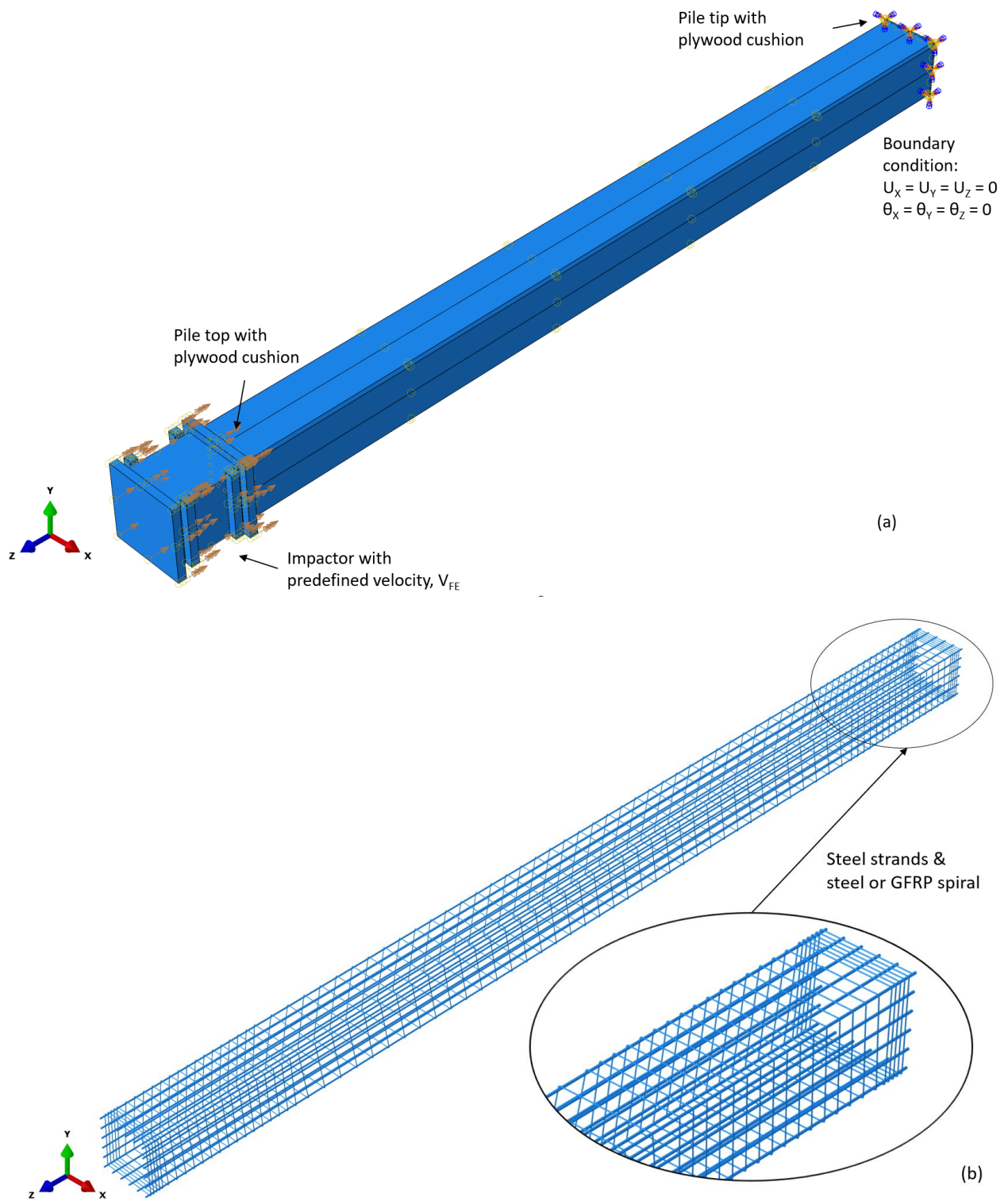Steel strands &
steel or GFRP spiral

(b)

Figure 2.3: (a) Test setup assembly in ABAQUS; (b) Reinforcement embedded in pile model

To account for these energy losses not modeled in the FE analysis, the energy-equivalent velocity $V_{FE} < V$ was assigned to the impactor. Based on the high-speed camera image analyses of all impact experiment conducted, the percentage of the initial potential energy lost only due to centripetal force on the pendulum mechanism after impact ranged between 23% to 26%. To account for this and other energy loss scenarios, the energy-equivalent velocity V_{FE} was estimated for a specific drop height by multiplying the original impact velocity V with a reduction factor α as shown in Equation (2.2). The reduction factor α accounted for the non-linear relationship between energy loss and test drop height.

$$V = \sqrt{2gh} \tag{2.1}$$

$$V_{FE} = \alpha V \tag{2.2}$$

where h is the impactor drop height, and g is gravitational constant. As shown in Table 2.1, the reduction was greater for lower drop heights because the aforementioned energy losses took a larger portion of the total impact energy. For example, closing of the gap between the plywood cushion and the pile would be more pronounced at lower heights than greater heights.

Table 2.1: Reduction factor for estimating energy-equivalent velocity in FE

Drop height (ft.)	Reduction factor (α)	Energy-equivalent velocity(V_{FE}) (ft./s)
4	0.476	7.64
7	0.480	10.19
10	0.528	13.40
15	0.652	20.27
20	0.809	29.01

Recall, the model of the pile impact experiment consisted of the pile concrete, steel strands, steel or GFRP spirals, a steel impactor and plywood cushions. The concrete, impactor and plywood cushions were modeled with C3D8R type elements. C3D8R is an 8-node linear brick element with reduced integration (1 integration point) and each node having three degrees of freedom. The

concrete had a total of 15,680 elements with 18,193 nodes, whereas the impactor had a total of 2,876 elements with 4,238 nodes. Each pile cushion also had 144 elements with 338 nodes.

The prestressing strands, steel wire spiral and GFRP spiral were modeled as three-dimensional 2-node truss elements (T3D2). For all 20 prestressing strands, there were 3,360 elements with 3,380 nodes. The steel wire spiral and GFRP spiral had 2,965 and 2959 elements with 2,966 and 2960 nodes, respectively. Therefore, for the FE impact analysis of PSS with one plywood cushion each at the top and tip of the pile, the total number of elements was 21,809, while for PSG1 with two plywood cushions at the top and one plywood cushion at the tip, there were a total of 21,947 elements.

For the interaction between reinforcement assembly (strands and spiral) and concrete, the embedded region constraint was used. This assumed a perfect bond between the reinforcements and the concrete interface. This is a suitable approximation since there was very minimal movement between concrete and reinforcements during actual physical experiments.

The FE analyses conducted for the test piles involved the complementary use of ABAQUS implicit and explicit solvers. To achieve the prestressed state of the piles, prestressing was applied using the implicit solver. The stressed state was then imported to the explicit solver for dynamic analysis. ABAQUS explicit is generally used to solve high speed/ short duration dynamic problems, such as drop tests, automotive crash analysis and impact tests. The time step for the explicit analyses conducted was 0.1 milliseconds. Concrete mesh size was set to 3 in., while other components of the model had 2 in. size mesh.

2.3 Material models

2.3.1 Concrete material model

ABAQUS provides several constitutive models for simulating the behavior of concrete. The concrete damaged plasticity (CDP) model was selected for this research. The CDP model is a plasticity-based model suitable for the static and dynamic analysis of prestressed concrete (Chung et al.,2014; Mercan et al., 2010, 2016). CDP was firstly introduced by Lubliner et al. (1989) and later modified by Lee & Fenves (1998). The tensile and compressive response of concrete as characterized by CDP is shown in Figure 2.4. CDP model can take inputs for the stress-strain relations, damage parameters and strain rates in compression and tension.
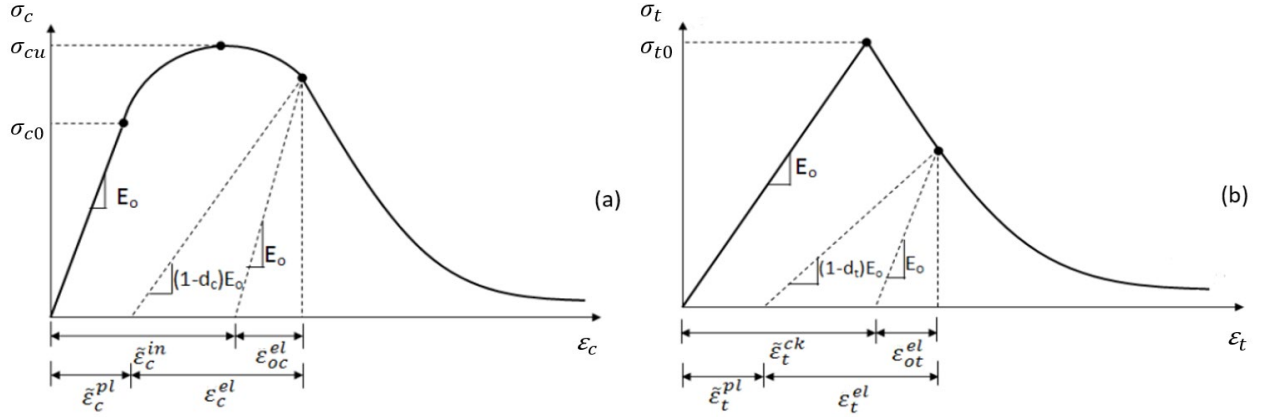
Figure 2.4: Stress-strain curve of concrete in (a) compression and (b) tension for the CDP model

Also, as shown in Figure 2.4, the CDP model considers the compressive crushing and tensile cracking modes of concrete failure through damage parameters d_c and d_t for compression and tension, respectively. The values for the damage parameters range from zero, which represents no damage, to one, which represents total damage and loss of material strength. Furthermore, the post-failure behavior of concrete in compression and tension, represented by the post-failure stress, is a function of the crushing strain $\tilde{\varepsilon}_c^{in}$ and cracking strain $\tilde{\varepsilon}_t^{ck}$, respectively. The crushing strain is calculated as the total strain minus the elastic strain that corresponds to the undamaged material as shown in Equation (2.3).

$$\tilde{\varepsilon}_c^{in} = \varepsilon_c - \varepsilon_{oc}^{el} = \varepsilon_c - \frac{\sigma_c}{E_0} \tag{2.3}$$

where ε_c is the total compressive strain, ε_{oc}^{el} is the elastic compressive strain, σ_c is the concrete compressive strength at any point and E_0 is the undamaged elastic modulus. The cracking strain on the other hand is calculated as shown in Equation(2.4).

$$\tilde{\varepsilon}_t^{ck} = \varepsilon_t - \varepsilon_{ot}^{el} = \varepsilon_t - \frac{\sigma_t}{E_0} \tag{2.4}$$

where ε_t is the total tensile strain, ε_{ot}^{el} is the elastic tensile strain, σ_t is the concrete tensile strength at any point.

The crushing and cracking strains calculated as described above is automatically converted to corresponding plastic strain values by the ABAQUS program as according to Equation (2.5) and Equation (2.6) below. Plastic strain values calculated using Equation (2.5) and Equation (2.6)

should neither be negative or of a decreasing value with increasing inelastic (crushing) strain or cracking strain values, otherwise, ABAQUS indicates an error.

$$\tilde{\varepsilon}_c^{pl} = \tilde{\varepsilon}_c^{in} - \left(\frac{d_c}{1 - d_c}\right)\left(\frac{\sigma_c}{E_0}\right) \tag{2.5}$$

$$\tilde{\varepsilon}_t^{pl} = \tilde{\varepsilon}_t^{ck} - \left(\frac{d_t}{1 - d_t}\right)\left(\frac{\sigma_t}{E_0}\right) \tag{2.6}$$

The input values of d_c and d_t under uniaxial compression and tension, respectively, can be approximated using Equation (2.7) and Equation (2.8) (Othman & Marzouk, 2018; Ren et al., 2015; Tao & Chen, 2015).

$$d_c = 1 - \frac{\sigma_c}{\sigma_{cu}} \tag{2.7}$$

$$d_t = 1 - \frac{\sigma_t}{\sigma_{t0}} \tag{2.8}$$

Also, for the CDP model, the mathematical formulation for the yield function, defined in terms of effective stresses, and the flow potential function are well explained Lubliner et al., (1989) ~~by~~ and Lee & Fenves, (1998). The parameters that must be defined for CDP are the dilation angle ψ, the flow potential eccentricity e, the ratio of initial biaxial compressive yield stress to initial uniaxial compressive yield stress σ_{b0}/σ_{c0}, the shape factor (or the ratio of the second stress invariant on the tensile meridian to compressive meridian at initial yield) K, and the viscosity parameter μ. The input CDP parameters utilized for the pile model are shown in Table 2.2. It should be noted that values for e, σ_{b0}/σ_{c0}, and K are default values.

Table 2.2: Concrete damaged plasticity (CDP) model parameters

Dilation angle ψ	Eccentricity e	σ_{b0}/σ_{c0}	K	viscosity parameter μ
30	0.1	1.16	0.667	0.0001

2.3.2 Concrete stress-strain curve

The stress-strain curve for concrete in compression suggested Collins & Mitchell (1991) was adopted in the numerical model as shown in Equations (2.9) to (2.16).

$$f_c = \left(\frac{n \left(\varepsilon_{cf}/\varepsilon_c' \right)}{n - 1 \left(\varepsilon_{cf}/\varepsilon_c' \right)^{nk}} \right) f_c' \qquad (2.9)$$

$$\varepsilon_c' = \frac{f_c'}{E_c} \frac{n}{n-1} \qquad (2.10)$$

$$k = \begin{cases} 1 & \text{if } \varepsilon_{cf} < \varepsilon_c' \\ 0.67 + \dfrac{f_c'}{9000} & \text{if } \varepsilon_{cf} \geq \varepsilon_c' \end{cases} \qquad (2.11)$$

$$n = 0.8 + \frac{f_c'}{2500} \qquad (2.12)$$

$$E_c = 40{,}000\sqrt{f_c'} + 1{,}000{,}000 \qquad (2.13)$$

where ε_{cf} is the concrete compressive strain; f_c is the concrete compressive strength at ε_{cf} (psi); f_c' is the concrete compressive strength (psi); ε_c' is the strain corresponding to compressive strength; k and n are factors given in Equation (2.11) and (2.12); and E_c is the elastic modulus of concrete (psi). The modulus of elasticity of concrete E_c was correlated to its compressive strength using Equation (2.13) and the Poisson's ratio was defined as 0.2. Figure 2.5 shows the stress-strain curve for concrete behavior in compression.

Also, the behavior of concrete in tension was modeled using Equations (2.14) to (2.16) as recommended by Belarbi & Hsu, (1994).

$$f_t = \begin{cases} E_c \, \varepsilon_t & \text{if } \varepsilon_{cf} \leq \varepsilon_c' \\ f_{cr} \left(\dfrac{\varepsilon_{cr}}{\varepsilon_t} \right)^{0.4} & \text{if } \varepsilon_{cf} > \varepsilon_c' \end{cases} \qquad (2.14)$$

$$\varepsilon_{cr} = \frac{f_{cr}}{E_c} \qquad (2.15)$$

$$f_{cr} = 4\sqrt{f_c'} \qquad (2.16)$$

where ε_t is the concrete tensile strain; f_t is the concrete tensile stress at ε_t (psi); ε_{cr} is the cracking strain of concrete in tension; and f_{cr} is cracking stress of concrete in tension (psi). The stress-strain curve for defining the tensile behavior of the concrete is as shown in Figure 2.6.

The mechanical properties of the concrete used in the FE model are summarized in Table 2.

Table 2.3: Mechanical properties of concrete

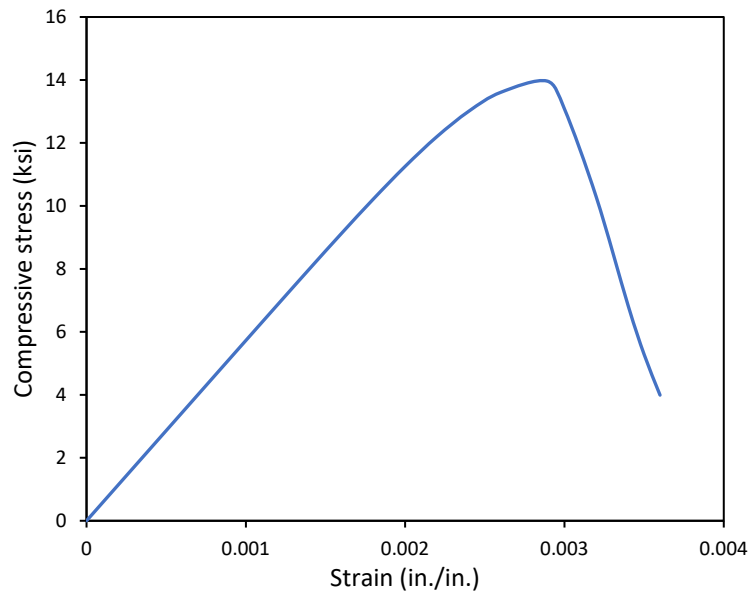| Density	f_c'	f_{cr}	E_c	ν
lbf s^2/in^4	ksi	ksi	ksi	
2.24e-04	13.9	0.47	5727	0.2

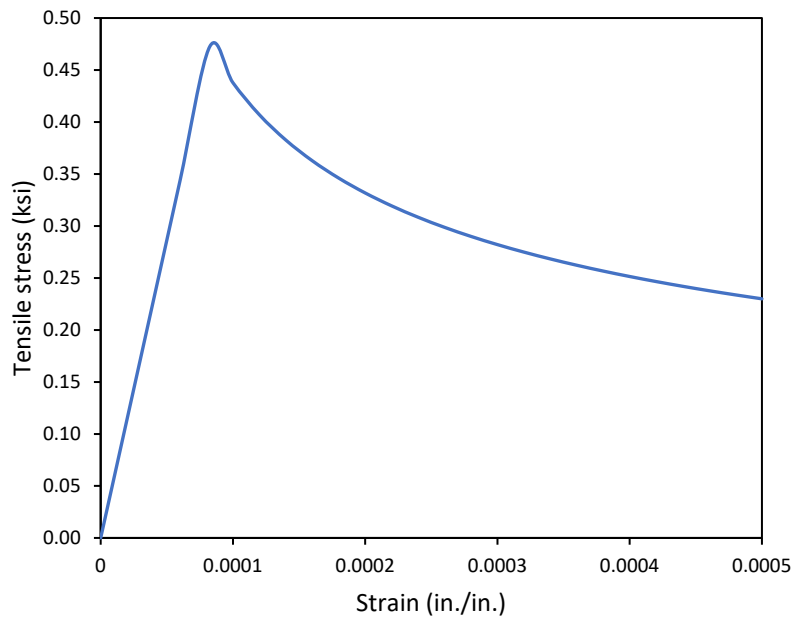*Figure 2.5: Concrete stress-strain curve in compression*

Figure 2.6: Concrete stress-strain curve in tension

2.3.3 Prestressing strand, steel wire and GFRP material model

Two types of steel reinforcements were used namely, Grade 270 low relaxation prestressing strands and a steel wire spiral. The stress-strain curve for prestressing steel proposed by Devalapura et al. (1992) was used in this study as shown in Figure 2.7. The equation for this curve is expressed as

$$f_{ps} = \varepsilon_{ps} \left[A + \frac{B}{\left\{ 1 + \left(C\varepsilon_{ps} \right)^D \right\}^{1/D}} \right] \leq f_{pu} \tag{2.17}$$

where f_{ps} is the stress in the prestressing strand corresponding to a given strain ε_{ps}; f_{pu} is the maximum strand stress and A, B, C, and D are constants obtained by curve fitting. For a 270 ksi low-relaxation steel strand the constants are equal to 887, 27613, 112.4 and 7.360, respectively. These values of f_{ps} are sensitive to these constants, therefore, the values of the constants should not be rounded.
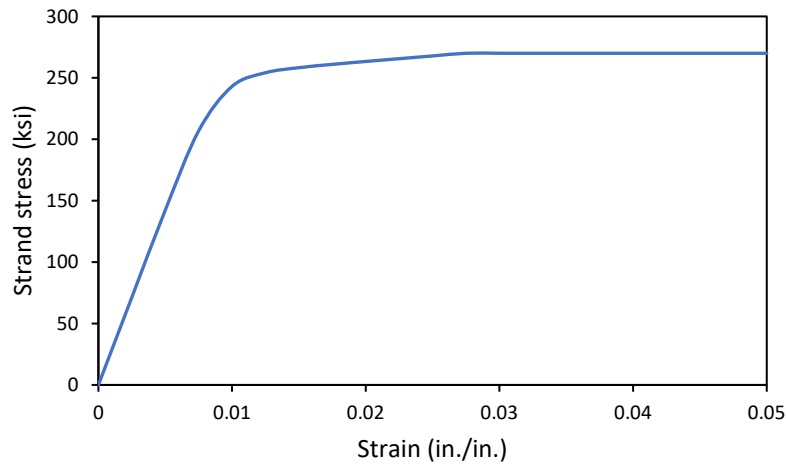

Figure 2.7: Stress-strain curve for prestressing steel strands

For the steel wire spiral, a bilinear stress-strain curve with an elastic and strain hardening portion was used to model its behavior, as shown in Figure 2.8. E_s, f_y and f_u represent the elastic modulus, the yield strength, and the ultimate strength of the steel wire, respectively.

GFRP exhibits elastic-brittle behavior, therefore the GFRP spiral was modeled as a linear elastic material until failure. In ABAQUS, a very small value of 1.00e-05 was assigned for the plastic

strain to failure (Almusallam et al., 2013). The properties of the prestressing strand, steel wire and GFRP spirals are summarized in Table 2.4.

Table 2.4: Mechanical properties of reinforcement

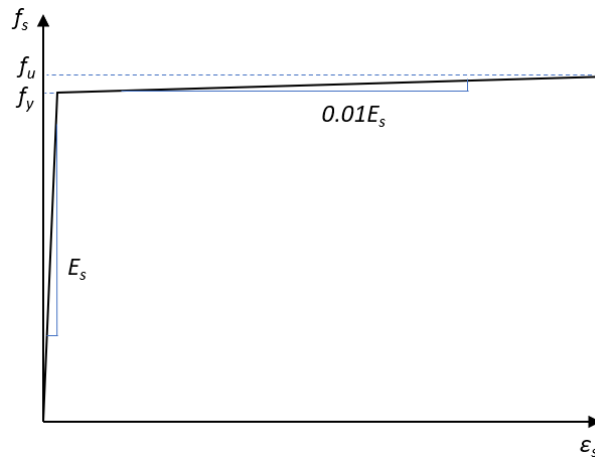| Reinforcement type	Area in.^{2}	ρ lbf s^2/in^4	$E_{ps}/E_s/E_f$ ksi	f_{py}/f_y ksi	$f_{pu}/f_u/f_{fu}$ ksi	v
Prestressing strand	0.167	7.3e-04	28,500	243	270	0.3
Steel wire spiral	0.034	7.3e-04	29,000	70	80	0.3
#3 GFRP spiral	0.11	1.97e-04	6,500	—	120	0.25

Figure 2.8: Stress-strain curve for steel wire spiral

2.4 Application of prestress

The modeling of a prestressed concrete member in ABAQUS/explicit requires that the state of initial stress in the member be appropriately created at the beginning of the analysis. The prestressing force can either be defined directly by prescribing an initial stress that is assumed to be constant along the length of the strands or indirectly by introducing an artificial temperature drop in the strands. The initial stress state in the pile was obtained by the direct method of prestress application in the ABAQUS implicit solver. This initial stress state was imported to the ABAQUS explicit solver for further analysis. The alternative method of applying the prestressing force was through a predefined temperature reduction according to Equation (2.18).

$$\Delta T = - \frac{f_{pe}}{\alpha_{ps} E_{ps}} \tag{2.18}$$

where ΔT is the required temperature reduction, f_{pe} is the effective prestress in the strands after loss, α_{ps} is the coefficient of thermal expansion in the strands taken as 1.15×10^{-5} /°C and E_{ps} is the elastic modulus of the prestressing strands.

2.5 Comparison of test results to FE model results

Sample plots from the FE analysis are discussed first, before comparing them to the test results. Figure 2.9 shows axial stress plots at 4 different time steps for the PSS pile. Upon impact, the stress wave begins from the pile top (Figure 2.9a), propagating to the pile tip (Figure 2.9b, c). The stress wave is reflected at the tip and propagates backward (Figure 2.9d).
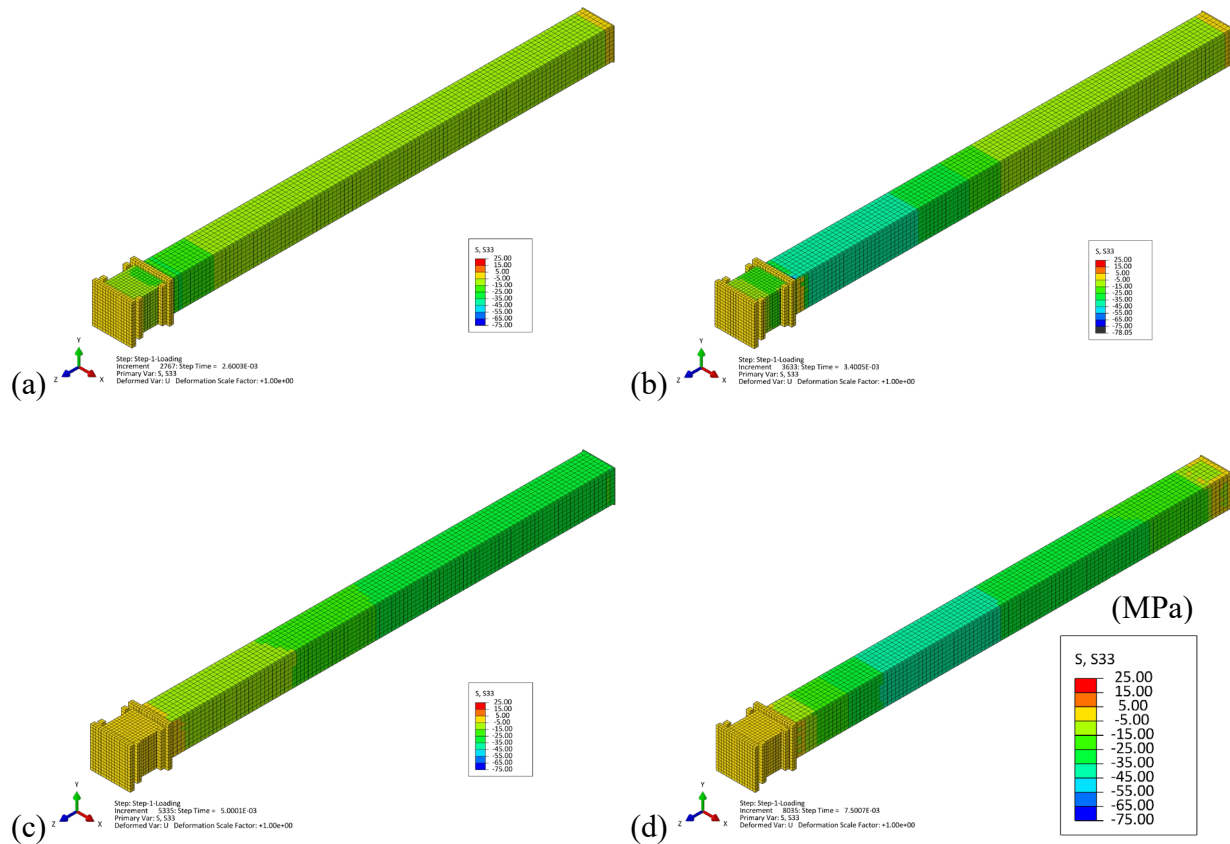

Figure 2.9: Stress propagation after impact, the PSS pile, 15 ft. drop height. (a), (b), (c) forward propagation (t = 0 0026, 0.0034, and 0.0050 sec), and (d) reflection and backward propagation (t = 0.0075 sec)

19

Figure 2.10 shows the stress at the pile head at the times steps t = 0.003 and 0.004 seconds for the PSS pile. As expected, the pile head surface experienced localized high stress of approximately 9 ksi, even though immediately away from the pile head the peak stress was approximately 5 ksi. The PSG1 pile showed similar behavior as shown in Figure 2.11.
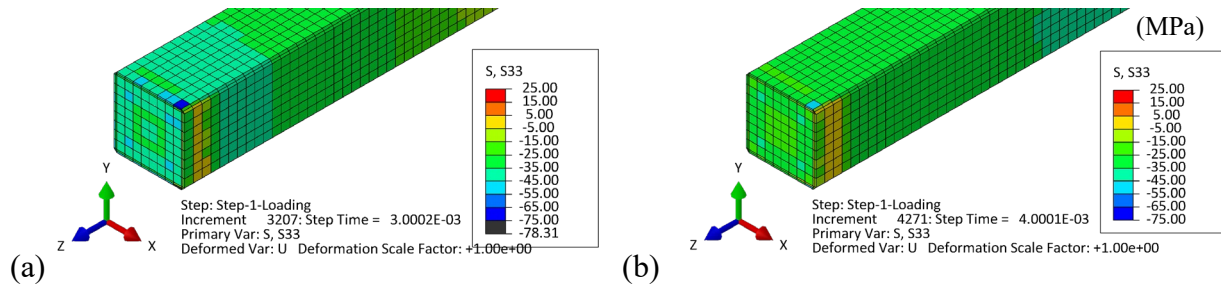

Figure 2.10: Stress at the pile top, the PSS pile, 15 ft. drop height. (a) t = 0.003 sec, (b) t = 0.004 sec

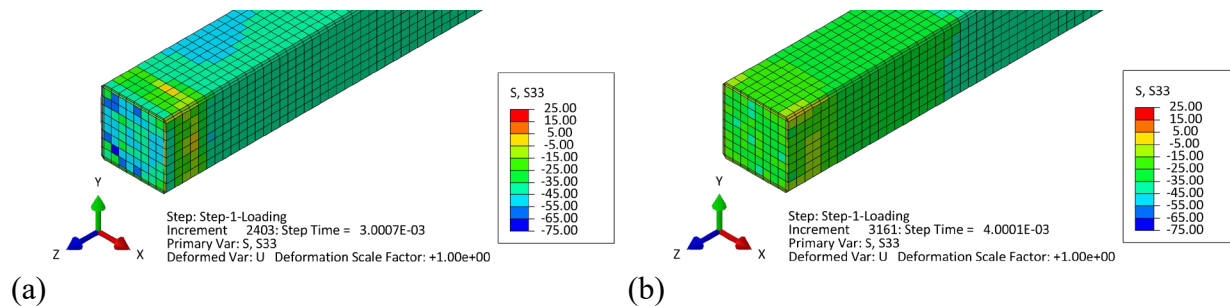*Figure 2.11: Stress at the pile top, the PSG1 pile, 20 ft. drop height. (a) t = 0.003 sec, (b) t = 0.004 sec*

Next, the FE analyses are compared to the test results. To compare the concrete stress on the surface, the value at 4 ft from the pile head was used. Figure 2.12 and Figure 2.13 show the time history of the stress for the PSS pile and the PSG1 pile. For each case, the maximum stress was recorded and compared to the testing results as shown in Figure 2.14 and Figure 2.15. The FE analysis showed a much better match (< 4% difference) than the analytical model discussed in the previous section. The FE stress was obtained from the result file. The experimental stress was obtained from the PDA measurements. The stress from both sides (east, west) were averaged to obtain the maximum stress.
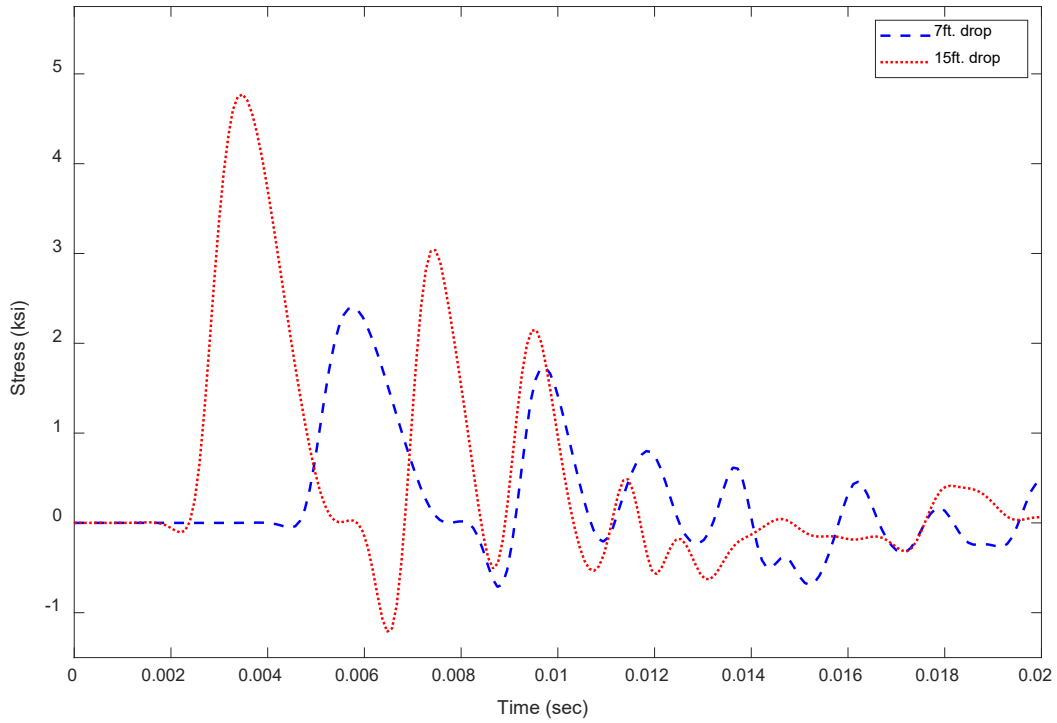
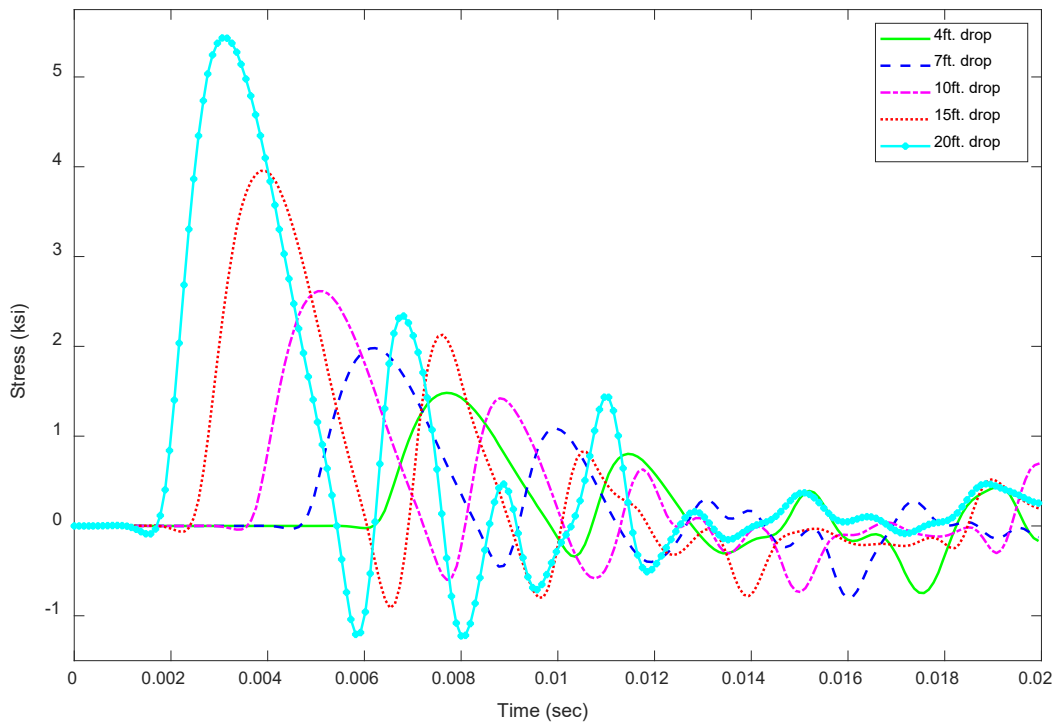*Figure 2.12: PSS FE stress plot (concrete stress on the surface, 4 ft from the top)*

Figure 2.13: PSG1 FE stress plot (concrete stress on the surface, 4 ft from the top)
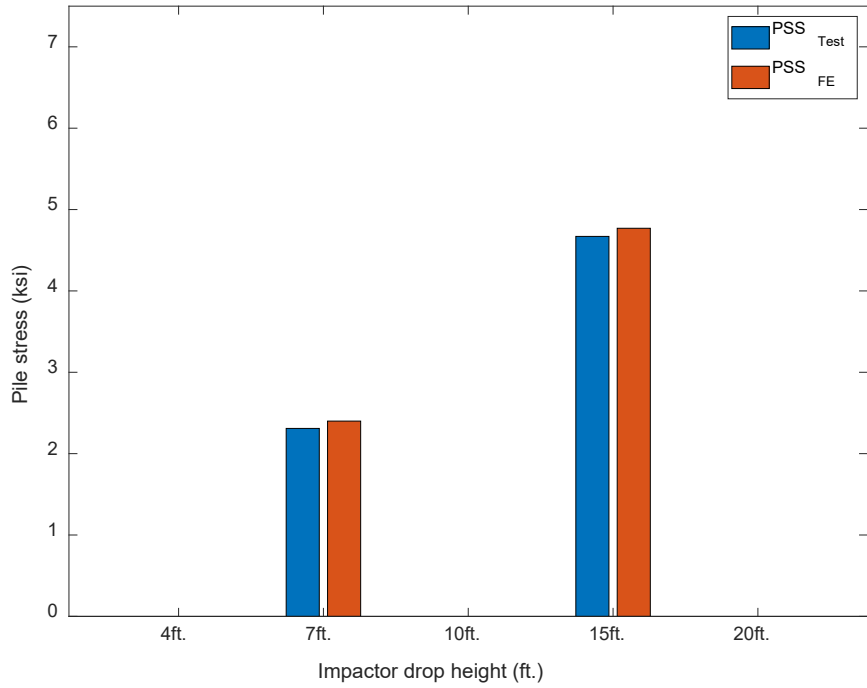
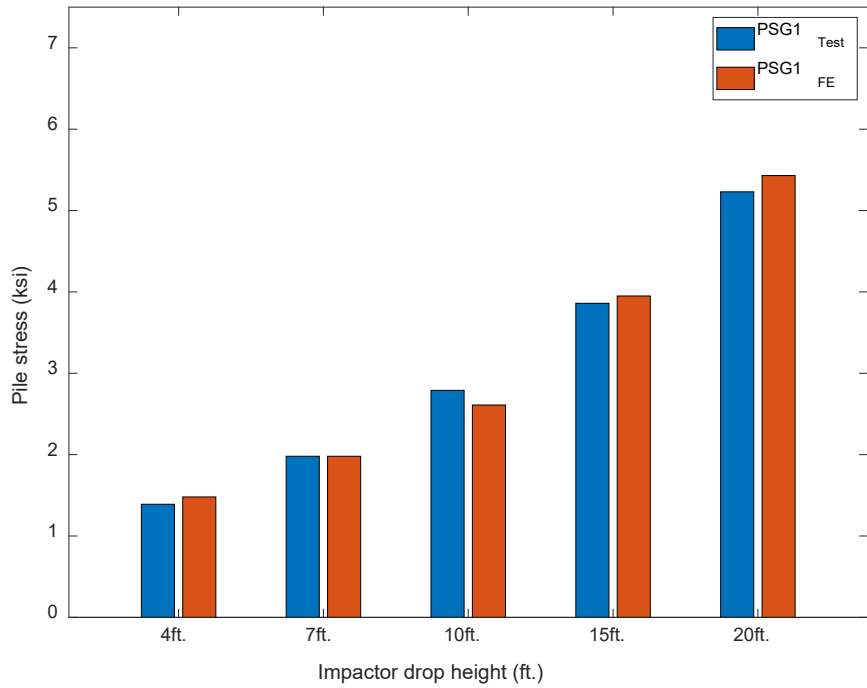*Figure 2.14: Comparison of test pile stress results to FE stress results (PSS)*

Figure 2.15: Comparison of test pile stress results to FE stress results (PSG1)

Figure 2.16 and Figure 2.17 compare the spiral strain between the test results and the FE analyses. The test results were reproduced from the Task 4D report. Unlike the test results, the FE analyses were nearly symmetric between the east and the west side, so only one side was used in the plot. The legend "FE" indicates the strain at the same location as the testing, whereas the legend "FE corner strain" indicates the strain from the round corner that exhibited a larger value for some locations. The following can be observed from the figures.

- Overall, the FE strain was much lower than the strains observed in the PSS testing. Recall that the PSS specimen's end surface was not flush with the cushion and caused flexural failure, as evidenced by un-symmetric strain response (also see the photos of the Task 4D report, section 3.1.4). The large strains of the PSS testing were due to this issue. On the other hand, the FE model was under axial impact loading only and produced smaller strains.

- For the PSS specimen, the pile head strain was still a good match between the east side of the testing and the FE result.

- For the PSG1 pile, the FE strain overall matched closely with the testing results. The peak strain at the pile head was particularly a good match to the west side testing results. On the other hand, the FE results were much lower than the two localized peaks observed in the east side of the testing specimen.

- Due to the completely fixed boundary condition of the FE analysis, the strain amplification at the pile tip was about 2.5 times of the pile head strain (vs. about 1.5 times amplification for the testing). The amplified strain, however, was still lower than the limit as shown in the figure.
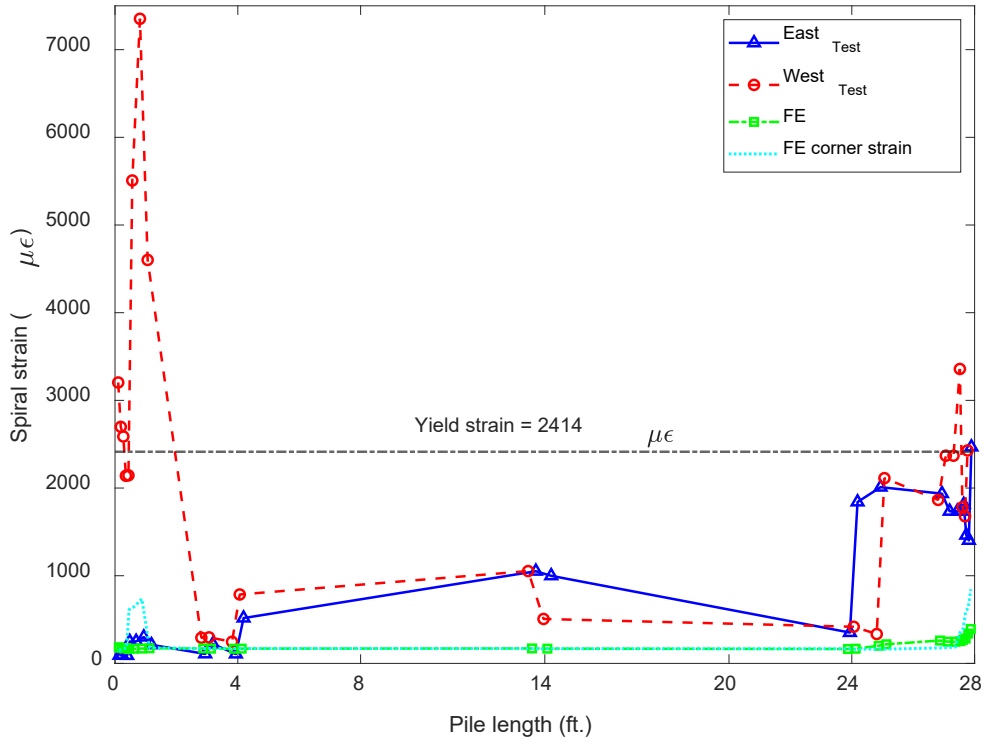
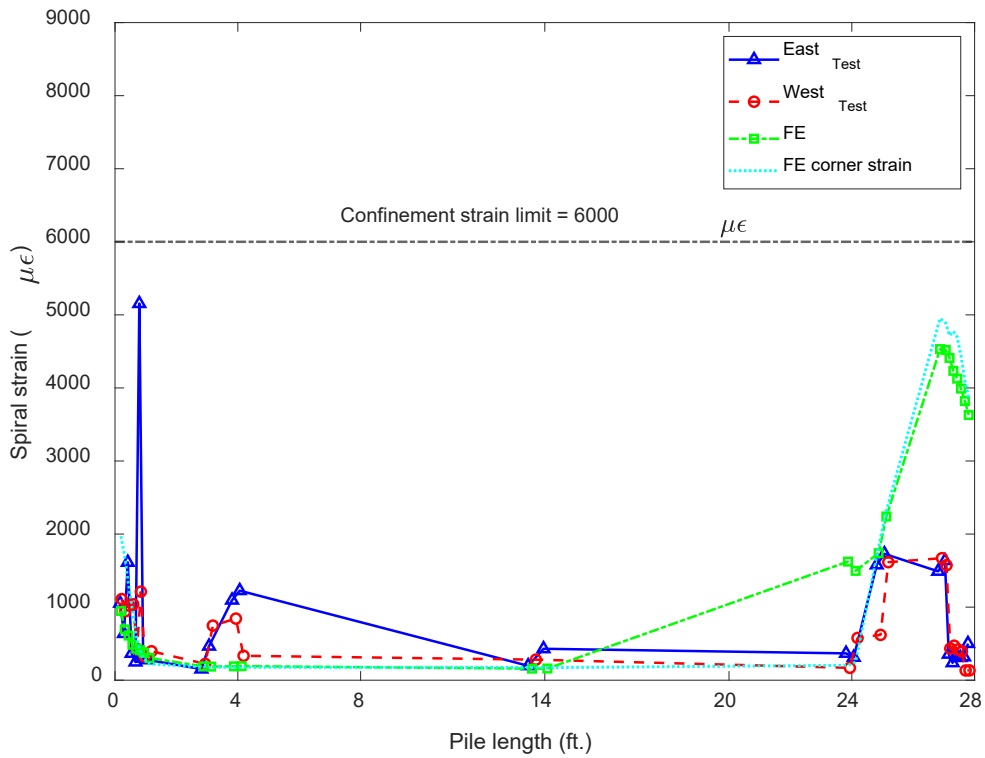*Figure 2.16: Test vs FE steel spiral strain for PSS (15 ft. drop height)*

Figure 2.17: Test vs FE steel spiral strain for PSG1 (20 ft. drop height)

Bibliography

Almusallam, T. H., Elsanadedy, H. M., Al-Salloum, Y. A., & Alsayed, S. H. (2013). Experimental and numerical investigation for the flexural strengthening of RC beams using near-surface mounted steel or GFRP bars. *Construction and Building Materials*, *40*, 145–161.

Belarbi, A., & Hsu, T. T. (1994). Constitutive laws of concrete in tension and reinforcing bars stiffened by concrete. *ACI Structural Journal*, *91*(4), 465–474.

Chung, C. H., Lee, J., & Gil, J. H. (2014). Structural performance evaluation of a precast prefabricated bridge column under vehicle impact loading. *Structure and Infrastructure Engineering*, *10*(6), 777–791.

Collins, M. P., & Mitchell, D. (n.d.). *PreStressed Concrete Structures*. Prentice Hall, Englewood Cliffs, NJ.

Devalapura, R. K., Tadros, M. K., & Prewett, C. W. (1992). Stress-Strain Modeling of 270 ksi Low-Relaxation Prestressing Strands. *PCI Journal*, *37*(2), 100–106.

Lee, J., & Fenves, G. L. (1998). Plastic-Damage Model for Cyclic Loading of Concrete Structures. *Journal of Engineering Mechanics*, *124*(8), 892–900.

Lubliner, J., Oliver, J., Oller, S., & Oñate, E. (1989). A plastic-damage model for concrete. *International Journal of Solids and Structures*, *25*(3), 299–326.

Mercan, B., Schultz, A. E., & Stolarski, H. K. (2010). Finite element modeling of prestressed concrete spandrel beams. *Engineering Structures*, *32*(9), 2804–2813.

Mercan, B., Stolarski, H. K., & Schultz, A. E. (2016). Arc-length and explicit methods for static analysis of prestressed concrete members. *Computers and Concrete*, *18*(1), 17–37.

Othman, H., & Marzouk, H. (2018). Applicability of damage plasticity constitutive model for ultra-high performance fibre-reinforced concrete under impact loads. *International Journal of Impact Engineering*, *114*, 20–31.

Ren, W., Sneed, L. H., Yang, Y., & He, R. (2015). Numerical Simulation of Prestressed Precast Concrete Bridge Deck Panels Using Damage Plasticity Model. *International Journal of Concrete Structures and Materials*, *9*(1), 45–54.

Tao, Y., & Chen, J. F. (2015). Concrete Damage Plasticity Model for Modeling FRP-to-Concrete Bond Behavior. *Journal of Composites for Construction*, *19*(1).